


Orthotopic Versus Allotopic Implantation: Comparison of Radiological and Pathological Characteristics

YeYu Cai, PhD,¹ TaiLi Chen, PhD,² JiaYi Liu, PhD,¹ ShuHui Peng, PhD,¹ Huan Liu, MD,¹ Min Lv, MD,¹ ZhuYuan Ding, MD,¹ ZiYi Zhou, MD,¹ Lan Li, PhD,³ Shan Zeng, PhD,^{2*} and EnHua Xiao, PhD^{1,4,5*} 

Background: In experimental animal models, implantation location might influence the heterogeneity and overall development of the tumor, leading to an interpretation bias.

Purpose: To investigate the effects of implantation location in experimental tumor model using magnetic resonance imaging (MRI) and pathological findings.

Study Type: Prospective.

Subjects: Forty-five breast cancer-bearing mice underwent orthotopic ($N = 15$) and heterotopic (intrahepatic [$N = 15$] and subcutaneous [$N = 15$]) implantation.

Field Strength/Sequence: Sequences including: T1-weighted turbo spin echo sequence, T2-weighted blade sequence, diffusion-weighted imaging, pre- and post-contrast T1 mapping, multi-echo T2 mapping at 3.0 T.

Assessment: MRI was performed at 7, 14, and 21 days after implantation. Native T1, post-contrast T1, T2, and apparent diffusion coefficient (ADC) of tumors, the tumor volume and necrosis volume within tumor were obtained. Lymphocyte cells from H&E staining, Ki67-positive, and CD31-positive cells from immunohistochemistry were determined.

Statistical Tests: One-way analysis of variance and Spearman's rank correlation were performed. P value < 0.05 was considered statistically significant.

Results: The tumor volume (intrahepatic vs. orthotopic vs. subcutaneous: $587.50 \pm 77.62 \text{ mm}^3$ vs. $814.00 \pm 43.85 \text{ mm}^3$ vs. $956.13 \pm 119.22 \text{ mm}^3$), necrosis volume within tumor ($89.10 \pm 26.60 \text{ mm}^3$ vs. $292.41 \pm 57.92 \text{ mm}^3$ vs. $179.91 \pm 31.73 \text{ mm}^3$, respectively), ADC at day 21 (543.41 ± 42.28 vs. 542.92 ± 99.67 vs. 369.83 ± 42.90 , respectively), and post-contrast T1 at all time-points (day 7: 442.00 ± 11.52 vs. 435.00 ± 22.90 vs. 394.33 ± 29.95 ; day 14: 459.00 ± 26.11 vs. 436.83 ± 26.01 vs. 377.00 ± 27.83 ; day 21: 463.50 ± 23.49 vs. 458.00 ± 34.28 vs. 375.00 ± 30.55) were significantly different between three groups. Necrosis volumes of subcutaneous and intrahepatic tumors were significantly lower than those of orthotopic tumors. The CD31-positive rate in the intrahepatic implantation was significantly higher than in orthotopic and subcutaneous groups. Necrosis volume ($r = -0.71$), ADC ($r = -0.85$), and post-contrast T1 ($r = -0.75$) were strongly correlated with vascular invasion index.

Data Conclusion: Orthotopic and heterotopic tumors have their unique growth kinetics, necrosis volume, and vascular invasion. Non-invasive MR quantitative parameters, including ADC and post-contrast T1, may reflect vascular invasion in mice.

Level of Evidence: 1

Technical Efficacy: Stage 3

J. MAGN. RESON. IMAGING 2022;55:1133–1140.

Tumor heterogeneity is thought to play an important role in tumor growth and treatment.¹ Although cancer formation is a clonal process, not all malignant cells within a tumor exhibit the same characteristics.² Inter-tumor heterogeneity refers to the difference found between tumors in different individuals.³ This is the focus of many cancer studies, including

View this article online at wileyonlinelibrary.com. DOI: 10.1002/jmri.27940

Received Jul 12, 2021, Accepted for publication Sep 14, 2021.

*Address reprint requests to: S.Z. or E.X., Changsha 410011, China. E-mail: zengshan2000@csu.edu.cn; xiaoenhua64@csu.edu.cn
YeYu Cai and TaiLi Chen contributed equally to this work.

From the ¹Department of Radiology, The Second Xiangya Hospital, Central South University, Changsha, China; ²Department of Oncology, Xiangya Hospital, Central South University, Changsha, China; ³Department of Pathology, The Second Xiangya Hospital, Central South University, Changsha, China; ⁴Molecular Imaging Research Center, Central South University, Changsha, China; and ⁵Clinical Research Center for Medical Imaging in Hunan Province, Changsha, China

This is an open access article under the terms of the Creative Commons Attribution-NonCommercial-NoDerivs License, which permits use and distribution in any medium, provided the original work is properly cited, the use is non-commercial and no modifications or adaptations are made.

those on alterations in cancer driver genes and those on differences in patient response to therapy.^{4,5} Compared with inter-tumor heterogeneity, studies on intra-tumor heterogeneity have focused not only on identifying genetic differences between tumor cells,⁶ but also on features of the tissue micro-environment such as metabolism,⁷ immunity,^{8,9} and hypoxia.¹⁰

In laboratory studies, the animal model of transplanted tumors, which are formed by continuous passage of tumor cells to an animal from either the same or heterogeneous animal species, is the most used *in vivo* method.^{11,12} Conventional xenograft models represent the complexity of genetic and epigenetic abnormalities and are used to reduce inter-tumor heterogeneity by grafting the human tumor micro-environment.¹³ Syngeneic tumor models are immunocompetent models with relatively uniform growth, and are commonly utilized to evaluate intra-tumor heterogeneity.¹⁴ However, tumor location, which is important for determining the heterogeneity of tumor growth,¹⁵ has rarely been studied. Different locations within the body have specific histocytes, extracellular matrix compartments, or vasculature.¹⁶ These extrinsic factors, which affect the outgrowth of tumors, comprise the tumor micro-environment. Consequently, they could reinforce the heterogeneity of tumors and have a profound effect on overall tumor development. Another consideration is that there are two widely used types of transplanted tumor models (the orthotopic model and the heterotopic model). Each model has its own advantages. The subcutaneous model, as a representative of the heterotopic model, is easy to implant and subsequently palpable,¹⁷ but the

orthotopic model provides a tumor micro-environment that leads to the development of the distinct biological properties of tumor cells.¹⁸ Therefore, the selection of implantation location might influence the heterogeneity of the tumor, leading to an interpretation bias.

In cancer research, magnetic resonance imaging (MRI) has been used extensively to determine the size, location, vascular invasion, and tumor heterogeneity.¹⁹ This technique is well-tolerated by humans and laboratory animals and it has been shown that repeated study does not influence animal welfare or tumor growth.²⁰

Thus, the aim of this study was to investigate the effects of orthotopic and heterotopic (intrahepatic and subcutaneous) implantation in mouse models with highly vascularized and syngeneic 4T1 breast cancer using MRI.

Materials and Methods

Animal Experiments and Tumor Extraction

All animal experiments were performed in accordance with the guidelines of the Animal Care Committee. Maximum effort was maintained in minimizing animal distress. In total, 45 female BALB/c mice (aged 8–10 weeks) were purchased from the Laboratory Animal Center. They were housed under temperature-controlled conditions (20–26 °C) with a regular daylight cycle. The laboratory mice were provided *ad libitum* access to purified water and were fed a standard diet.

4T1 murine breast cancer cells (RPMI 1640 medium) were obtained from the Cell Bank of the Chinese Academy of Sciences (Shanghai, China). Orthotopic tumor inoculation was performed by injecting 100 μ L 4T1 cells (approximately 2×10^6 cells) into the right mammary fat pad of the mice. Tumor sizes were assessed daily using a Vernier caliper, and the volume was calculated using the following formula: $0.5 \times \text{length} \times (\text{width}^2)$. Afterwards, tumor tissues were obtained from 15 4T1-bearing donor mice. After achieving a tumor size of approximately 500 mm², the mice were euthanized, and the tumor was removed from the surrounding tissue. Next, the collected tumors were cleaned to remove necrotic tissue. Fish-like tumor tissues were soaked in a phosphate-buffered solution on ice and cut into small pieces (0.5–1.0 mm in diameter). Finally, the tumor tissue fragments were drawn into a 1-mL syringe.

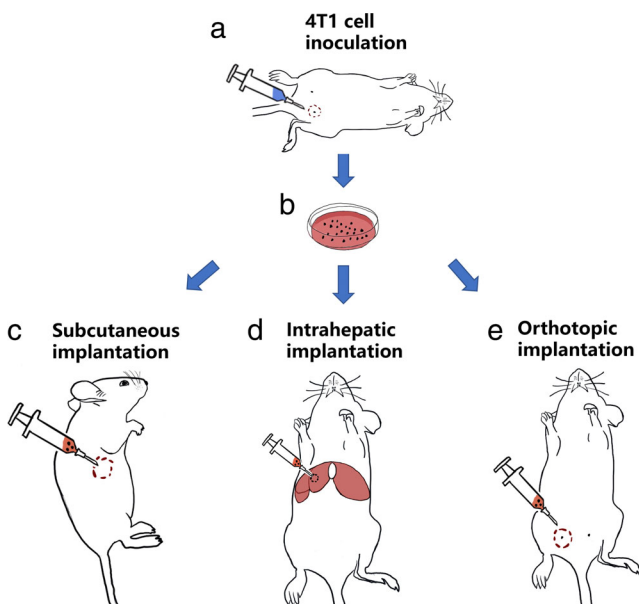


FIGURE 1: Workflow for the orthotopic and heterotopic tumor implantation. (a) 4T1 cells were inoculated at the breast. **(b)** Tumor tissues were extracted and cut into small pieces. **(c–e)** Tumor tissue fragments were drawn up into a 1-mL syringe with a 16G needle and were injected into the breast, skin, and liver in mice, separately.

Orthotopic and Heterotopic Tissue Implantation

All surgical procedures were performed while maintaining aseptic technique and keeping all instruments under sterile conditions. Forty-five mice were randomly divided into three groups: orthotopic, subcutaneous, and intrahepatic. All mice were prepared and disinfected for surgery after anesthetizing them with 50 mg/kg of pentobarbital sodium solution (Sigma, Shanghai, China) via intraperitoneal injection. Initially, the mice in the intrahepatic group were placed in the supine position on a heating pad. After confirming that adequate anesthesia was reached, the abdomens of the mice were opened by making a 1-cm right subcostal skin incision. The tumor fragments (0.1 mL) were subsequently injected into the parenchyma using a 16-G needle head while gently pressing the implantation location with a cotton swab. Finally, the liver was

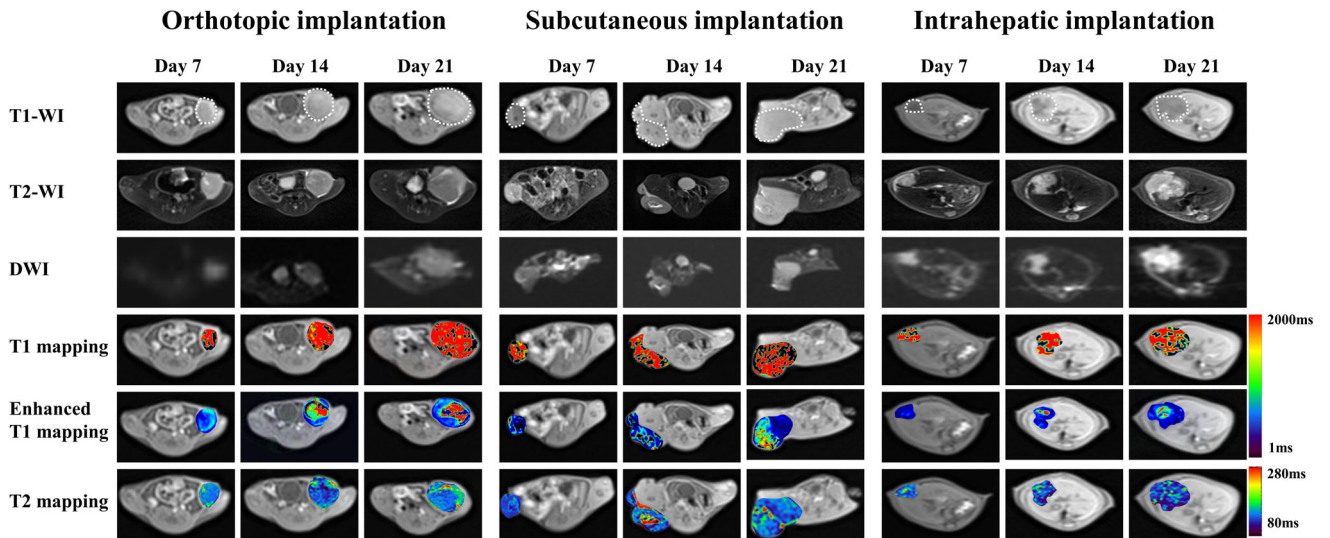


FIGURE 2: Example T1-weighted, T2-weighted, diffusion-weighted imaging (DWI), T1 mapping, enhanced T1 mapping, and T2 mapping images acquired at 7, 14, and 21 days after implantation. (a) Orthotopic implantation; (b) heterotopic subcutaneous implantation; (c) Heterotopic intrahepatic implantation. Example tumors represented as round or oval shape with mixed hyperintense T2-WI signal and hypointense T1-WI signal.

placed back into the abdominal cavity, and the skin was closed using absorbable sutures. The mice in the orthotopic and subcutaneous groups were administered orthotopic and subcutaneous injections with 0.1 mL of tumor fragments using a 16-G needle head into their right mammary fat pad and right flank. The time between the removal of the sample from the donors and tissue implantation did not exceed 30 min for each single mouse among all three groups.

MRI Protocol

Images were obtained using a 3.0-T MRI scanner (MAGNETOM Skyra, Siemens, Erlangen, Germany) with a custom-built animal coil (Zhongzhi Medical Technologies, Suzhou, China) at 7, 14, and 21 days after implantation. Before imaging, all mice were anesthetized with 50 mg/kg pentobarbital sodium solution via intraperitoneal injection. During imaging, unconscious movements were

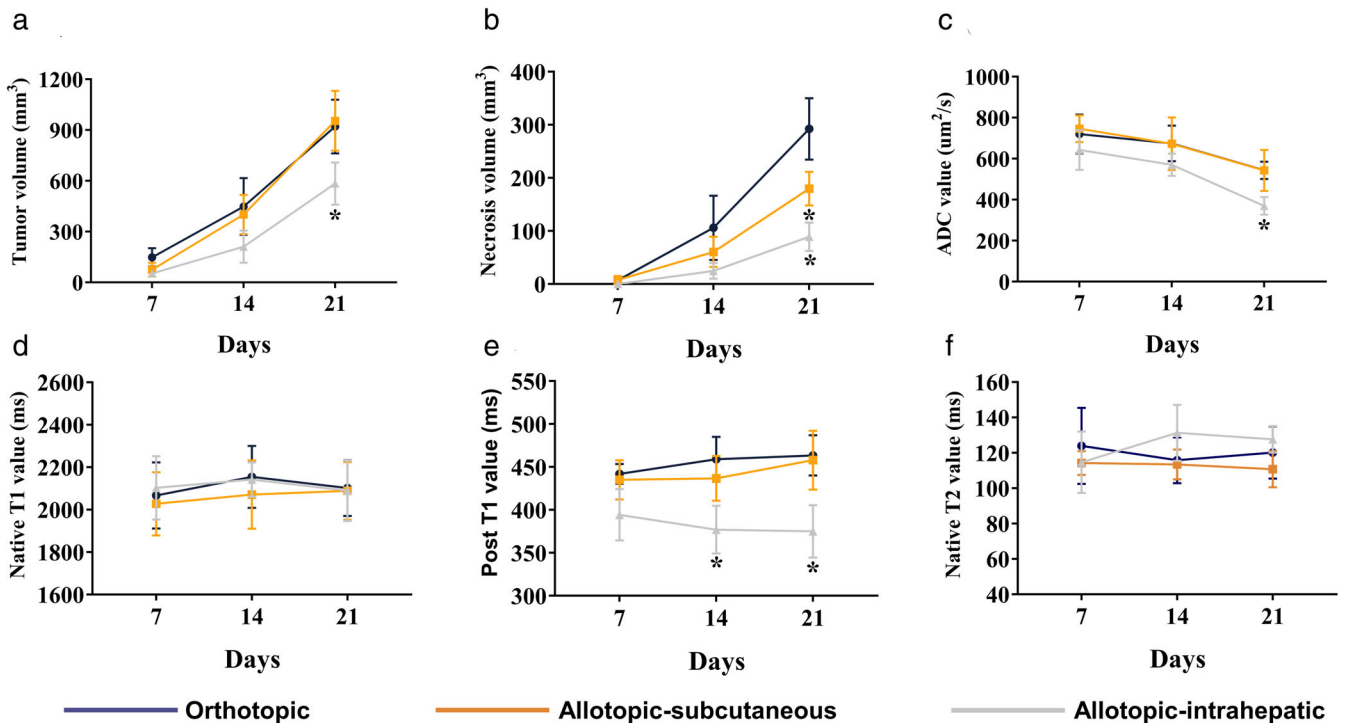


FIGURE 3: Quantitative and semi-quantitative analysis of multiparametric MR parameters at different time points. (a, b) Semi-quantitative analysis of tumor volume and necrosis volume. (c-f) Quantitative analysis of apparent diffusion coefficient (ADC), T1, post-T1, and T2 values.

TABLE 1. Comparison of the MR Parameters Between Orthotopic Implantation, Subcutaneous Implantation, and Intrahepatic Implantation Groups at 7, 14, and 21 Days

| MR Parameter | Day 7 | | | Day 14 | | | Day 21 | | | | | |
|--|------------------|------------------|------------------|------------|------------------|------------------|-----------------|--------------|------------------|------------------|------------------|----------|
| | Orthotopic | Subcutaneous | Intrahepatic | Orthotopic | Subcutaneous | Intrahepatic | Orthotopic | Subcutaneous | Intrahepatic | | | |
| Pre-T1 (msec) | 2067.05 ± 155.74 | 2027.52 ± 148.90 | 2103.07 ± 149.27 | 0.694 | 2154.65 ± 145.87 | 2071.19 ± 160.95 | 2141.90 ± 81.03 | 0.523 | 2101.76 ± 131.36 | 2088.65 ± 135.69 | 2089.33 ± 142.44 | 0.834 |
| Post-T1 (msec) | 442.00 ± 11.52 | 435.00 ± 22.90 | 394.33 ± 29.95 | 0.005* | 459.00 ± 26.11 | 436.83 ± 26.01 | 377.00 ± 27.83 | <0.001** | 463.50 ± 23.49 | 458.00 ± 34.28 | 375.00 ± 30.55 | <0.001** |
| T2 (msec) | 123.94 ± 21.47 | 114.25 ± 6.67 | 114.67 ± 17.36 | 0.417 | 115.81 ± 12.95 | 113.45 ± 8.41 | 131.33 ± 15.85 | 0.058 | 120.20 ± 14.74 | 110.72 ± 10.20 | 127.67 ± 7.53 | 0.059 |
| ADC (× 10 ⁻⁶ , mm ² /second) | 720.38 ± 94.80 | 746.00 ± 64.89 | 642.50 ± 96.80 | 0.133 | 674.52 ± 86.82 | 673.08 ± 128.18 | 570.38 ± 54.35 | 0.126 | 543.41 ± 42.28 | 542.92 ± 99.67 | 369.83 ± 42.90 | 0.003* |

ADC = apparent diffusion coefficient.
 * *P* < 0.05;
 ** *P* < 0.001.

monitored by periodic visual inspection via real-time circuit television.

The following MRI sequences were performed: 1) transverse T1-weighted turbo spin echo (TSE) sequence (repetition time [TR]/echo time [TE] = 3.3/1.7 msec, flip angle [FA] = 150°, slice thickness = 0.7 mm, field of view [FOV] = 90 mm × 90 mm, matrix = 448 × 448), acquisition time = 05:18; 2) transverse T2-weighted multi-shot motion-corrected radial TSE sequence (BLADE) (TR/TE = 5360.0/135 msec, FA = 160°, slice thickness = 0.7 mm, FOV = 100 mm × 100 mm, matrix = 384 × 384), acquisition time = 03:02; 3) diffusion-weighted imaging (DWI) using a multi-shot echo planar imaging sequence (TR/TE = 585.0/12.6 msec, slice thickness = 2 mm, FOV = 120 mm × 120 mm, matrix = 224 × 224, FA = 150°, *b*-values = 0 seconds/mm², 600 seconds/mm², and 800 seconds/mm²), acquisition time = 05:23; 4) T1 mapping using a modified Look-Locker sequence (TR/TE = 15.0/3.9 msec, FA = 6° and 15°, slice thickness = 0.8 mm), acquisition time = 03:55; and 5) multi-echo T2 mapping (TR = 1950 msec; TE = 11.1 msec, 22.2 msec, 33.3 msec, 44.4 msec, and 55.5 msec; FA = 180°, slice thickness = 1 mm), acquisition time = 06:30. For contrast-enhanced imaging, T1 mapping images were obtained immediately after the retro-orbital injection of 0.1 mL solution with 0.02 mL Magnevist (Bayer, Leverkusen, Germany) and 0.08 mL normal saline.

Imaging Analysis

All data were imported into a Syngo workstation (Siemens Medical Solutions, Erlangen, Germany) for measurement and analysis. From the images of routine T1-weighted and T2-weighted sequences in our study, we found the clear appearance of the tumor. Regions of interest (ROIs) were manually placed within the solid tumor region to measure the quantitative parameters from MR sequences. Two radiologists with over 10 years of experience (YHL, CM) and one radiologist with over 15 years of experience (QLS) performed the analysis. Both radiologists were blinded to the histopathological results. Quantitative MR parameters including apparent diffusion coefficient (ADC) values (× 10⁻⁶, mm²/second) from the DWI sequence, T1 values (msec) from the T1 mapping with and without contrast, and T2 values (msec) from the T2 mapping. The tumor volume (mm³) and inner necrotic volume (mm³) were determined at each time point by manually delineating the hyperintense tumor area on each two-dimensional slice in T2-weighted images and contrast-enhanced T1-weighted images. The volumes were estimated by adding the individual voxel volumes inside the corresponding regions while using smaller, more sharply defined voxels to decrease the partial volume effect on the boundaries of the surface. Special care was taken to avoid non-homogeneity within the ROI.

Histology and Immunohistochemistry

Mice were euthanized after the last MRI scan was performed by administering 150 mg/kg of pentobarbital sodium solution. Hematoxylin and eosin (H&E) staining was performed to assess lymphocyte infiltration and immunohistochemistry (CD31 and Ki67) staining was conducted to examine microvessel density and proliferation of tumor growth. The tumors were fixed in a 4% phosphate-buffered formaldehyde solution for 24 hours, embedded in paraffin, and sliced. Four-millimeter sections were then deparaffinized in

xylene and rehydrated in graded alcohols. Both H&E staining and immunohistochemistry (CD31 [GB12064, Servicebio, Wuhan, China] and Ki67 [GB111499, Servicebio, Wuhan, China]) staining were performed according to the standard protocols indicated by the manufacturers' instructions. The percentages of inflammation (lymphocyte cells (%) in H&E staining), cell proliferation (Ki67-positive cells (%) in immunohistochemistry), and vascular invasion (CD31-positive cells (%) in immunohistochemistry) per sample in three different fields were determined using a light microscopy system (DP72, Olympus Corporation, Tokyo, Japan) and ImageJ software (open source, NIH Image, USA).

Statistical Analysis

Statistical analyses were performed using SPSS (Version 22.0, SPSS Inc., Chicago, IL, USA). One-way analysis of variance (ANOVA) was used to analyze the differences between the orthotopic, subcutaneous, and intrahepatic groups. Correlation analysis was performed using Spearman's rank correlation coefficient (r). A P value <0.05 was considered statistically significant.

Results

Establishment of the Tumor Model and MRI Examination in Mice

Orthotopic, subcutaneous, and intrahepatic tumor models were successfully established in all the mice (Fig. 1). Figures 2 and 3

showed the images and quantitative parameters of tumors between three groups. Various degrees of hyperintensity were seen on DWI in the intrahepatic implanted tumor, brighter than those in the orthotopic and subcutaneous implanted tumors which were quantified by ADC values (hepatic vs. orthotopic vs. subcutaneous: $369.83 \pm 42.90 \times 10^{-6}$, $\text{mm}^2/\text{second}$ vs. $543.41 \pm 42.28 \times 10^{-6}$, $\text{mm}^2/\text{second}$ vs. $542.92 \pm 99.67 \times 10^{-6}$, $\text{mm}^2/\text{second}$, seen in Table 1). Tumor volume and necrosis volume increased slowly during the first 7 days post-implantation and then accelerated and reached their highest levels on day 21 in all groups (Fig. 3a,b). The intrahepatic implantation group had significantly lower tumor volume at day 21 than the other two groups (intrahepatic vs. orthotopic vs. subcutaneous: $587.50 \pm 77.62 \text{ mm}^3$ vs. $814.00 \pm 43.85 \text{ mm}^3$ vs. $956.13 \pm 119.22 \text{ mm}^3$). Additionally, on day 21, necrosis volumes of the subcutaneous and intrahepatic implantation groups were significantly lower than those of the orthotopic implantation group (intrahepatic vs. orthotopic vs. subcutaneous: $89.11 \pm 26.60 \text{ mm}^3$ vs. $292.41 \pm 57.92 \text{ mm}^3$ vs. $179.91 \pm 31.73 \text{ mm}^3$). ADC values (Fig. 3c) of the intrahepatic implantation group significantly decreased over time and at day 21 were significantly lower than those of the other two groups (shown in Table 1). Post-contrast T1 values (Fig. 3d) of the intrahepatic implantation group were

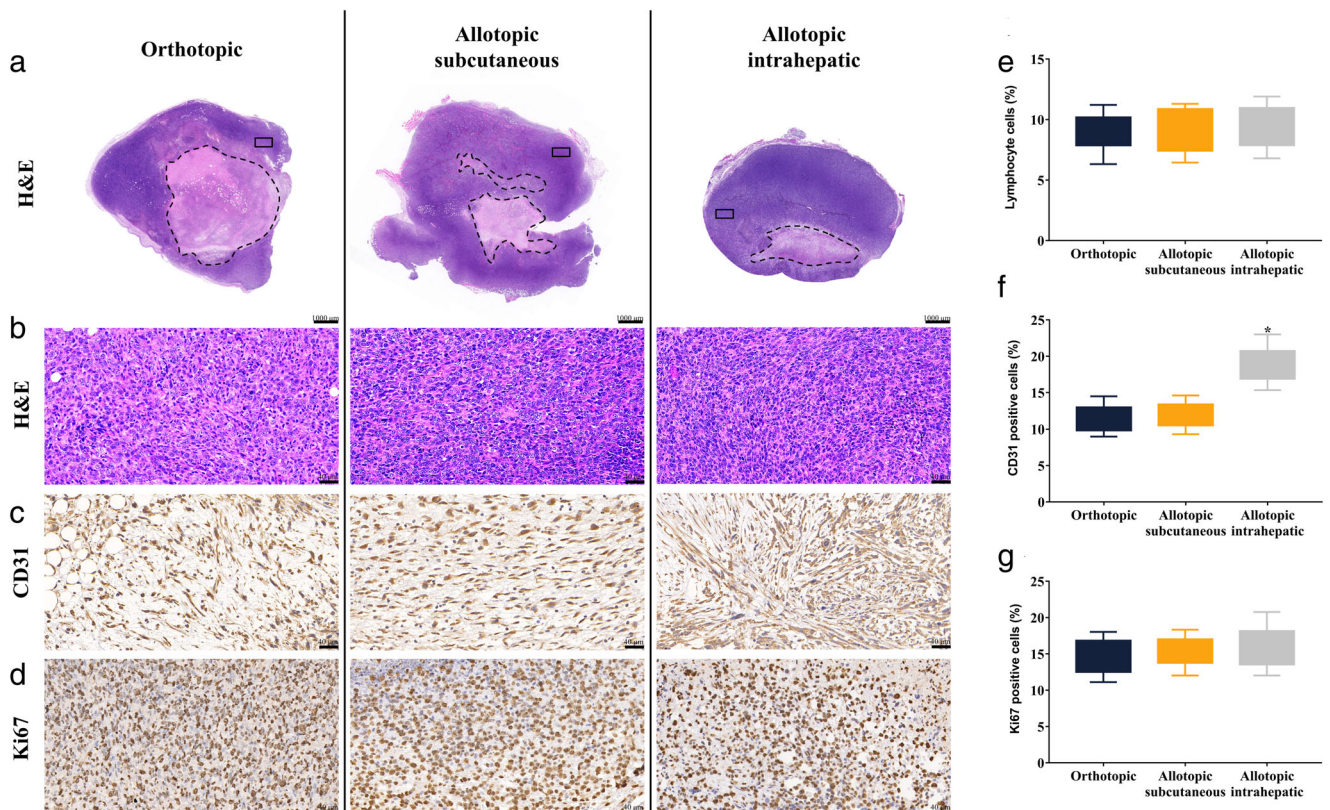


FIGURE 4: Typical histological images of slices from the orthotopic and allotopic groups. (a) Macroscopy of H&E staining (rectangular frame indicated the area of focused microscopy; broken line showed the area of necrosis). (b) Focused microscopy of H&E staining ($\times 400$) revealed lymphocyte infiltration. (c, d) Focused microscopy of CD-31 and Ki-67 staining ($\times 400$) manifested a positive stain in the membrane and nuclei of cells, respectively. (e–g) Quantitative analysis of lymphocyte, CD-31, and Ki-67 positive cells.

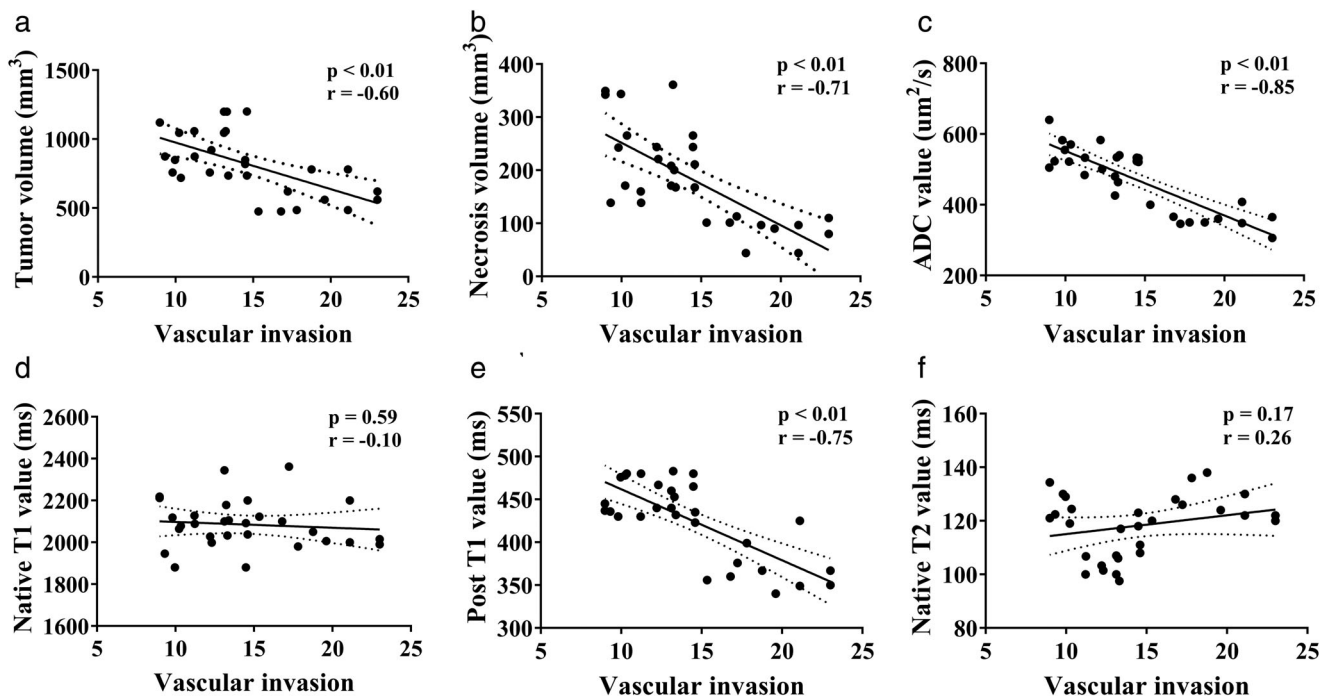


FIGURE 5: Scatterplots show the linear correlations between MR parameters ((a) tumor volume; (b) necrosis volume; (c) apparent diffusion coefficient (ADC) value; (d) T1 value; (e) post-T1 value; (f) native T2 value) and vascular invasion.

also significantly lower than those of the other two groups on days 14 and 21 (Table 1). However, no significant differences were observed in native T1 ($P = 0.694$, $P = 0.523$, $P = 0.834$, from day 7 to day 21) and T2 values ($P = 0.417$, $P = 0.058$, $P = 0.059$, from day 7 to day 21) among the three groups (Fig. 3e,f, Table 1).

Histological and Immunohistochemical Evaluation

Histological analysis revealed heterogeneity in the tumor micro-environment (Fig. 4). Macroscopic H&E staining showed uneven cell density and irregular necrosis. Although focused microscopy of H&E staining ($\times 400$) revealed the presence of lymphocyte infiltration, no significant differences were observed in the number of lymphocytes among the three groups ($P = 0.885$). Immunohistochemical analysis of CD31 showed a dark brown stain in the cell membrane, indicating the level of vascular invasion. The positivity rate of CD31 in the intrahepatic implantation group was significantly higher than that in the remaining groups ($P < 0.001$). Ki67 staining, a marker of cell proliferation, showed that the nuclei were stained dark brown. The percentage of Ki67 positive cells in the orthotopic implantation group was not significantly different from that in the allotopic-implantation group ($P = 0.462$).

Correlations Between MR Parameters and Vascular Invasion Index

The results of the correlation analysis (Fig. 5) between the MR parameters and vascular invasion index are shown in Fig. 5. Necrosis volume, ADC value, and post-contrast T1 value were strongly correlated with vascular invasion index ($r = -0.71$,

-0.85 , and -0.75 respectively). Tumor volume was moderately correlated with vascular invasion index ($r = -0.6$). However, native T1 and T2 values did not correlate with the vascular invasion index ($r = -0.1$, $P = 0.593$ and $r = 0.26$, $P = 0.173$ respectively).

Discussion

Tumor growth is a complex process that is characterized by many different aspects including implantation location. In this study, we investigated tumor location by using different surgical approaches to create orthotopic and heterotopic tumor models. MRI was subsequently used to investigate the heterogeneity of tumors at different implantation locations.

Compared with conventional cell suspensions that use tissue glue and tend to cause irregular tumor shapes and artificial remote metastasis, solid tumor implantation reduces inter-tumor heterogeneity because the tumor tissue preserves the micro-environment of the tumor during the transplantation process.^{21,22} In our study, we not only finished the implantation protocol within 10 min by using a 16-G needle, which was quicker than the 30 min surgery time mentioned in the previous study,²³ but also ensured a high success rate of implantation (100%).

In our study, the model tumors had similar characteristics between groups with a primarily homogeneous appearance. Moreover, the levels of proliferation and lymphocyte infiltration in the models were indistinguishable. This finding is contrary to that of previous studies performing cell suspension implantation, which suggested that the orthotopic model had a more suitable environment than the heterotopic model

in which the tumor cells proliferate or migrate.^{24,25} This could be due to the differences between the implants. However, our results showed that tumors from different implantation locations showed heterogeneity in tumor necrosis as well as in inflammatory and vascular invasion status *in vivo*. Surprisingly, orthotopic tumors had faster growth rates and larger volumes than heterotopic tumors in Fig. 3a. This inconsistency may be attributed to limitations in terms of growing space for intrahepatic tumors. Conversely, the vascular invasion in intrahepatic tumors was much higher than that in orthotopic tumors. This result supports the hypothesis that specific histocytes or vasculature in implantable locations could reinforce tumor heterogeneity. Since vascular endothelia can provide important information about the progression and prognosis of tumor,²⁶ there is a need for future investigations with more in-depth evaluation of the potential differences of orthotopic and heterotopic tumors in pre-clinical studies of contrast agents²⁷ and of drugs against common cancer types.²⁸

Non-invasive imaging studies are continuously being developed and are becoming more widely used. They have the important advantage of reducing animal usage as the imaging can be used to perform longitudinal monitoring in individual animals. In our study, we used a 3.0-T clinical MRI scanner with routine and functional sequences, which could be reliably applied for *in vivo* non-invasive characterization of tumors. Using this imaging data, the solid region and necrosis area within the tumor can be calculated to assess intra-tumor heterogeneity. Our study not only quantified the morphological characteristics of the tumor, but also correlated MRI results to immunohistochemical markers. Native T1 and T2 values of the tumor solid region do not correlate with the vascular invasion index. A possible explanation for T1 value might be that there were no obvious changes of intratumor ingredients including fat, air, and moving blood. Similarly, the differences of T2 value were not significant due to the stable intratumor composition including fat, fluids, and moving blood. However, there was a strong correlation between the post T1 value and intratumor vascular invasion, which suggested that the MRI could play an important role in assessing the level of intratumor vascular invasion. These relationships may partly be explained by the fact that the higher level of vascular invasion, the more filling the contrast agent during the arterial enhancement phase. ADC and post-contrast T1 values were strongly correlated with the vascular invasion index. These results are in accordance with those of recent studies that have indicated that non-invasive imaging findings could potentially be more accurate than some biological information, including the level of tissues, cells, or molecules.^{29–31}

Limitations

Firstly, a single cell line was used in this study. However, it seems feasible to use other cell lines in similar studies to avoid

selection bias. Secondly, metastasis might be more common in orthotopically implanted tumors because of their high fidelity to the actual implantation environment. Owing to the limited image resolution offered by MRI, micro-metastases have yet to be studied further. Finally, respiratory monitoring techniques are difficult to apply to mice, and respiratory movement during abdominal imaging may have decreased our image quality. However, we applied medical tapes to restrict these movements and obtain satisfactory results.

Conclusion

Our results show that orthotopic and heterotopic implantation presents unique micro-environments that influence growth kinetics, necrosis volume, and vascular invasion. MR quantitative parameters, including ADC and post-contrast T1 values, may noninvasively reflect vascular invasion indices in mice.

Acknowledgments

The authors acknowledge and thank Yongheng Luo (YHL), Cong Ma (CM), and Quanliang Shang (QLS) for reviewed and assessed MR images in the study. This study was supported by the National Natural Science Foundation of China (81601471; 81571784) and Provincial Natural Science Foundation of Hunan (2019JJ40434).

Conflict of Interest

All authors declare that they have no conflicts of interest.

References

1. Zhang Z, Liu L, Ma C, Cui X, Lam RHW, Chen W. An *in silico* glioblastoma microenvironment model dissects the immunological mechanisms of resistance to PD-1 checkpoint blockade immunotherapy. *Small Methods* 2021;5:2100197. <https://doi.org/10.1002/smt.202100197>.
2. Hayford CE, Tyson DR, Robbins CJ, Frick PL, Quaranta V, Harris LA. An *in vitro* model of tumor heterogeneity resolves genetic, epigenetic, and stochastic sources of cell state variability. *PLoS Biol* 2021;19:e3000797. <https://doi.org/10.1371/journal.pbio.3000797>.
3. Cusnir M, Cavalcante L. Inter-tumor heterogeneity. *Hum Vaccin Immunother* 2012;8:1143-1145. <https://doi.org/10.4161/hv.21203>.
4. Molina-Sánchez P, Ruiz de Galarreta M, Yao MA, et al. Cooperation between distinct cancer driver genes underlies intertumor heterogeneity in hepatocellular carcinoma. *Gastroenterology* 2020;159:2203-2220. <https://doi.org/10.1053/j.gastro.2020.08.015>.
5. Di J, Yang H, Jiang B, Wang Z, Ji J, Su X. Whole exome sequencing reveals intertumor heterogeneity and distinct genetic origins of sporadic synchronous colorectal cancer. *Int J Cancer* 2018;142:927-939. <https://doi.org/10.1002/ijc.31140>.
6. Karthikeyan S, Waters IG, Dennison L, et al. Hierarchical tumor heterogeneity mediated by cell contact between distinct genetic subclones. *J Clin Invest* 2021;131:e143557. <https://doi.org/10.1172/jci.143557>.
7. Liu X, Locasale JW. Metabolomics reveals intratumor heterogeneity – Implications for precision medicine. *EBioMedicine* 2017;19:4-5. <https://doi.org/10.1016/j.ebiom.2017.04.030>.
8. Miething C, Scudippo C, Bosbach B, et al. PTEN action in leukaemia dictated by the tissue microenvironment. *Nature* 2014;510:402-406. <https://doi.org/10.1038/nature13239>.

9. Zhang X, Lin A, Han QY, et al. Intratumor heterogeneity of HLA-G expression in cancer lesions. *Front Immunol* 2020;11:559-565. <https://doi.org/10.3389/fimmu.2020.565759>.
10. Wang Y, Zhang Y, Huang Y, et al. Intratumor heterogeneity of breast cancer detected by epialleles shows association with hypoxic microenvironment. *Theranostics* 2021;11:4403-4420. <https://doi.org/10.7150/thno.53737>.
11. Brighi C, Reid L, Genovesi LA, et al. Comparative study of preclinical mouse models of high-grade glioma for nanomedicine research: The importance of reproducing blood-brain barrier heterogeneity. *Theranostics* 2020;10:6361-6371. <https://doi.org/10.7150/thno.46468>.
12. Troiani T, Schettino C, Martinelli E, Morgillo F, Tortora G, Ciardiello F. The use of xenograft models for the selection of cancer treatments with the EGFR as an example. *Crit Rev Oncol Hematol* 2008;65:200-211. <https://doi.org/10.1016/j.critrevonc.2007.10.003>.
13. Chen X, Shen C, Wei Z, et al. Patient-derived non-small cell lung cancer xenograft mirrors complex tumor heterogeneity. *Cancer Biol Med* 2021;18:184-198. <https://doi.org/10.20892/j.issn.2095-3941.2020.0012>.
14. Liu J, Li Y, Zhang J, et al. Comparison of anesthesia and tumor implantation methods for establishing rabbit VX2 hepatocarcinoma. *Am J Transl Res* 2019;11:7157-7165.
15. Serie DJ, Joseph RW, Cheville JC, et al. Clear cell type a and B molecular subtypes in metastatic clear cell renal cell carcinoma: Tumor heterogeneity and aggressiveness. *Eur Urol* 2017;71:979-985. <https://doi.org/10.1016/j.eururo.2016.11.018>.
16. Árnadóttir SS, Mattesen TB, Vang S, et al. Transcriptomic and proteomic intra-tumor heterogeneity of colorectal cancer varies depending on tumor location within the colorectum. *PLoS One* 2020;15:e0241148. <https://doi.org/10.1371/journal.pone.0241148>.
17. Rubio-Manzanares Dorado M, Gómez LMM, Sánchez DA, et al. Translational pancreatic cancer research: A comparative study on patient-derived xenograft models. *World J Gastroenterol* 2018;24:794-809. <https://doi.org/10.3748/wjg.v24.i7.794>.
18. Trimaglio G, Tilkin-Mariamé AF, Feliu V, et al. Colon-specific immune microenvironment regulates cancer progression versus rejection. *Oncotargets Ther* 2020;9:101-125. <https://doi.org/10.1080/2162402x.2020.1790125>.
19. Taoka T, Jost G, Frenzel T, Naganawa S, Pietsch H. Impact of the lymphatic system on the kinetic and distribution of gadodiamide in the rat brain: Observations by dynamic MRI and effect of circadian rhythm on tissue gadolinium concentrations. *Invest Radiol* 2018;53:529-534. <https://doi.org/10.1097/rli.0000000000000473>.
20. Baier J, Rix A, Drude NI, et al. Influence of MRI examinations on animal welfare and study results. *Invest Radiol* 2020;55:507-514. <https://doi.org/10.1097/rli.0000000000000669>.
21. Feng F, Cheng Q, Li B, et al. Establishment and characterization of 38 novel patient-derived primary cancer cell lines using multi-region sampling revealing intra-tumor heterogeneity of gallbladder carcinoma. *Hum Cell* 2021;34:918-931. <https://doi.org/10.1007/s13577-021-00492-5>.
22. Chervoneva I, Peck AR, Yi M, Freydin B, Rui H. Quantification of spatial tumor heterogeneity in immunohistochemistry staining images. *Bioinformatics (Oxford, England)* 2021;37:1452-1460. <https://doi.org/10.1093/bioinformatics/btaa965>.
23. Kim MP, Evans DB, Wang H, Abbruzzese JL, Fleming JB, Gallick GE. Generation of orthotopic and heterotopic human pancreatic cancer xenografts in immunodeficient mice. *Nat Protoc* 2009;4:1670-1680. <https://doi.org/10.1038/nprot.2009.171>.
24. Erstad DJ, Sojoodi M, Taylor MS, et al. Orthotopic and heterotopic murine models of pancreatic cancer and their different responses to FOLFIRINOX chemotherapy. *Dis Model Mech* 2018;11:dmm034793. <https://doi.org/10.1242/dmm.034793>.
25. Yao X, Hu JF, Daniels M, et al. A novel orthotopic tumor model to study growth factors and oncogenes in hepatocarcinogenesis. *Clin Cancer Res* 2003;9:2719-2726.
26. Chand M, Evans J, Swift RI, et al. The prognostic significance of post-chemoradiotherapy high-resolution MRI and histopathology detected extramural venous invasion in rectal cancer. *Ann Surg* 2015;261:473-479. <https://doi.org/10.1097/sla.0000000000000848>.
27. Ren Y, Sedgwick AC, Chen J, et al. Manganese(II) texaphyrin: A paramagnetic photoacoustic contrast agent activated by near-IR light. *J Am Chem Soc* 2020;142:16156-16160. <https://doi.org/10.1021/jacs.0c04387>.
28. Bibby MC. Orthotopic models of cancer for preclinical drug evaluation: Advantages and disadvantages. *Eur J Cancer* 2004;40:852-857. <https://doi.org/10.1016/j.ejca.2003.11.021>.
29. Delli Pizzi A, Mastrodicasa D, Marchioni M, et al. Bladder cancer: Do we need contrast injection for MRI assessment of muscle invasion? A prospective multi-reader VI-RADS approach. *Eur Radiol* 2021;31:3874-3883. <https://doi.org/10.1007/s00330-020-07473-6>.
30. Gennaro N, Reijers S, Bruining A, et al. Imaging response evaluation after neoadjuvant treatment in soft tissue sarcomas: Where do we stand? *Crit Rev Oncol Hematol* 2021;160:303-309. <https://doi.org/10.1016/j.critrevonc.2021.103309>.
31. Pigeon H, Pérès EA, Truillet C, et al. TSPO-PET and diffusion-weighted MRI for imaging a mouse model of infiltrative human glioma. *Neuro Oncol* 2019;21:755-764. <https://doi.org/10.1093/neuonc/noz029>.